

Quantum Hall Effect Measurement of Spin-Orbit Coupling Strengths in Ultraclean Bilayer Graphene/WSe₂

Heterostructures

Dongying Wang¹, Shi Che¹, Guixin Cao¹, Rui Lyu², Kenji Watanabe³, Takashi Taniguchi³, Chun Ning Lau¹, Marc Bockrath^{1}*

¹Department of Physics, The Ohio State University, Columbus, OH 43210, USA

²Department of Physics and Astronomy, University of California, Riverside, CA 92521, USA

³National Institute for Materials Science, Namiki Tsukuba Ibaraki 305-0044 Japan.

KEYWORDS: graphene, transition-metal dichalcogenide, spin-orbit coupling, quantum transport

ABSTRACT

We study proximity-induced spin-orbit coupling (SOC) in bilayer graphene/few-layer WSe₂ heterostructure devices. Contact mode atomic force microscopy (AFM) cleaning yields ultra-clean interfaces and high-mobility devices. In a perpendicular magnetic field, we measure the quantum Hall effect to determine the Landau level structure in the presence of out-of-plane Ising and in-plane Rashba SOC. A distinct Landau level crossing pattern emerges when tuning the charge density and displacement field independently with dual gates, originating from a layer-selective SOC proximity effect. Analyzing the Landau level crossings and measured inter-Landau level energy gaps yields the proximity induced SOC energy scale. The Ising SOC is ≈ 2.2 meV, 100 times higher than the intrinsic SOC in graphene, while its sign is consistent with theories predicting a dependence of SOC on interlayer twist angle. The Rashba SOC is ~ 15 meV. Finally, we infer the magnetic field dependence of the inter-Landau level Coulomb interactions. These ultraclean bilayer graphene/WSe₂ heterostructures provide a high mobility system with the potential to realize novel topological electronic states and manipulate spins in nanostructures.

Efforts to control spin and electronic ground state topology in devices has driven an intensive study of spin-orbit coupling in materials.^{1,2} Graphene is a two-dimensional (2D) material with excellent electronic properties but small spin-orbit coupling (SOC),³⁻⁶ motivating efforts to increase it.⁷⁻²¹ For example, adatoms such as hydrogen or transition metals increase graphene's SOC,^{7,8} however these add disorder and lower charge mobility.⁷ In another approach, coupling graphene to 2D materials with strong SOC such as transition metal dichalcogenides also increases graphene's SOC,^{9-16, 18, 19, 21} while the interfacing of two crystalline systems adds less intrinsic disorder. Such studies have shown weak antilocalization signatures of spin-orbit coupling^{9, 10, 13-16} as well as spin Hall signatures.¹² However, electrical transport studies in high mobility devices on the quantum Hall effect are limited, which can act as a precise probe of the SOC in graphene, and potentially realize new topological ground states.^{19, 20, 22} Moreover, while recent progress has been made by a combination of capacitance and some transport measurements,²² inter-Landau level energy gaps have not been measured, nor the Rashba SOC or magnetic field dependence of the inter-Landau level Coulomb interactions.

Here we report coupling bilayer graphene (BLG) via layer stacking to WSe₂, a 2D semiconductor with strong SOC, in hexagonal BN (hBN) encapsulated devices. We obtain high mobility devices ($\sim 110,000 \text{ cm}^2\text{V}^{-1}\text{s}^{-1}$) by squeezing contaminants away from device areas using contact AFM.²³ Our devices are dual gated, allowing independent tuning of the charge density n and perpendicular displacement field D . At low temperatures under a perpendicular magnetic field B , we observe the quantum Hall effect (QHE) with all degeneracies lifted for $D = 0$, resulting from inversion symmetry breaking by the WSe₂ layer contacting the graphene.

Applying a nonzero D yields a finite interlayer potential difference, enabling us to observe Landau level (LL) crossings²⁴⁻²⁸ that differ in D values from isolated BLG.

To understand this behavior, we compare our results to a single-particle theory that includes an out-of-plane Ising SOC λ as well as an in-plane Rashba SOC λ_R .²⁰ For the nearly degenerate zero energy Landau level octet, most crossings deviate from the single-particle picture due to Coulomb interactions, except for the $\nu = \pm 3$ crossings.^{20, 22, 29} From these we extract $\lambda \sim -2.2$ meV, where the sign indicates the direction of the effective out-of-plane magnetic field from the SOC in the bilayer graphene at the K point of the Brillouin zone (with the opposite direction at the K' point).²⁰ consistent with recent theoretical work predicting that λ can be negative depending on the graphene/WSe₂ twist angle.³⁰ To gain further insight into the device behavior, we measure the inter-LL gaps using temperature-dependent transport measurements. These gaps are potentially affected by both the Landau level width as well as Coulomb interactions. We therefore study the rate of gap closure with displacement field, which is independent of these within a Hartree-Fock model. Measuring these rates for several gaps, we find the best fit to the measured values using the Rashba SOC as a fit parameter, yielding $\lambda_R \approx 15$ meV.

Using this λ_R value, we then compare the measured gap evolution with B for $\nu = 5, 6,$ and 7 to the single particle theory. The $\nu = 5$ and 7 gaps' behavior is close to the theory predictions, while the $\nu = 6$ gap shows significant deviations. From these deviations we determine the Coulomb interactions representing the exchange splitting for opposite spins for states deriving from the K and K' points. We find that the interaction energy scales vary approximately linearly with B over the measured range, consistent with previously found behavior.^{31, 32} The $\nu = 5$ and $\nu = 7$ gaps differ slightly, which may originate from differences in exchange energy due to the

Rashba coupling. Finally, we compare the crossing points to the single particle model, using λ_R as a fit parameter, which yields 20 meV, somewhat larger but in reasonable agreement to that found using the gap closing rates. This suggests that the crossing points not too strongly affected by Coulomb interactions.

Our devices were fabricated using a dry transfer and stacking method.³³ Both BLG and few-layer WSe₂ flakes were first exfoliated from bulk crystals, and then stacked and encapsulated between atomically flat hBN layers. The interlayer BLG/WSe₂ twist angle was $\sim 15^\circ$ as determined by the layer edge alignment. After transfer, the stack was deposited on a Si wafer capped with 285 nm of SiO₂ and vacuum annealed at 360°C for one hour. To further promote the interlayer coupling of BLG and WSe₂, we used an AFM tip to controllably squeeze out trapped contaminants from the stack.²³ A clean region was identified by AFM and the rest was etched by a mixture of CHF₃ (40 sccm) and O₂ (4 sccm) gas into a Hall bar geometry. After the etch process, Cr/Au (5nm/70nm) electrodes were deposited to make one-dimensional edge contacts,³³ and a metal top gate was added by an Al₂O₃/Au deposition step.

The Figure 1(a) left inset shows an optical image of the device before the top gate fabrication (located within the dotted rectangle), while the Figure 1(a) right inset shows the layer stacking diagram. Completed devices were measured in a variable-temperature flowing gas ⁴He cryostat. All four-terminal resistance measurements were performed with standard lock-in methods at a base temperature ~ 1.5 K unless noted. We used the highly-doped silicon substrates as a global bottom gate. In conjunction with the top gate, this device geometry allows independent control of the carrier density [$n = (C_{BG}V_{BG} + C_{TG}V_{TG})/e - n_0$, where C_{BG} and C_{TG} are the bottom and top gate capacitance per area, V_{BG} and V_{TG} are the bottom and top gate voltage, respectively, e is the electron charge and n_0 is residual charge due to doping] and the

applied displacement field [$D = (C_{\text{BG}}V_{\text{BG}} - C_{\text{TG}}V_{\text{TG}})/2\epsilon_0 - D_0$, where D_0 is the residual displacement field].

The longitudinal resistance R_{xx} vs. V_{BG} with $V_{\text{TG}} = 0$ is shown in the Figure 1(a) main panel. From this data, we determine the carrier mobility to be $\sim 110,000 \text{ cm}^2\text{V}^{-1}\text{s}^{-1}$ at low temperature, comparable to the high mobility achieved in typical BLG/BN systems. Under the application of a magnetic field, a color plot of R_{xx} vs. n and B shows a Landau fan pattern [Figure 1(b)], consistent with the QHE in bilayer graphene observed previously [see Supporting Information (SI) Figure S1 for more details]. The primary gaps occur at filling factors $\nu = \pm 4m$, where m is an integer. This is accounted for by the bilayer LL spectrum, given by

$E_N = \pm \hbar\omega\sqrt{N(N-1)}$, where $\omega = qB/m$ with q the electric charge and m the effective mass, and N is the orbital quantum number index.^{34,35} These LLs are fourfold degenerate due to spin and valley degeneracies, but are split by perturbations such as interactions and Zeeman splitting.^{36,37} Analyzing the QHE data, we extract the values of gate capacitances $C_{\text{BG}} = 13.5 \text{ nF/cm}^2$ and $C_{\text{TG}} = 72.5 \text{ nF/cm}^2$. For B larger than 6 T, we observe all integer QHE states, indicating the high quality of our sample.

To investigate the layer-selective spin-orbit proximity coupling, we studied the effects of varying D . The Figure 1(c) lower panel shows a color plot of R_{xx} vs. n and D , taken at $B = 10$ T. Similar data at $B = 6$ and 8 T are shown in SI Figure S2. (An artifact likely due to contact resistance and possible formation of resistive p - n junctions causes a downward-sloping feature in the plot obscuring the QHE signatures, especially at high B . An example of one of these features is marked by a white arrow. Here, we focus on the data outside this region.) The Figure 1(c) upper panel shows R_{xx} plotted vs. n for $D = 0$, yielding a series of R_{xx} minima due to the LLs in the BLG. All the odd filling states are present at $D = 0$ in contrast to BLG without WSe₂.^{27,28} As

D varies at fixed n , some of the R_{xx} minima vanish and then reemerge, indicating the closing and reopening of inter-LL gaps at LL crossing points. In Figure 1(d), line traces of R_{xx} minima at $\nu = 5$ and 6 fillings show peaks at particular D values, enabling extraction of the crossing points. Although the $\nu = 7$ curve does not go through a maximum in selected range, the upwards slope suggests a crossing point exists near $D = -0.15$ V/nm. As we find that R_{xy} is impacted less than R_{xx} by the contact artifact (see Figure S3), to ensure accuracy, we also calculate the derivative of R_{xy} with respect to n . This produces similar peaks as D varies, enabling the extraction of the same D values for the LL crossings.

The $N = 0, 1$ LLs in an isolated bilayer are degenerate in the single particle picture except for Zeeman splitting, but interactions lift all degeneracies.^{24, 29, 36, 38-41} Adding SOC is expected to modify both the inter-LL gaps and crossing points. We zoom in to the $dR_{xy}/d\nu$ vs. D and n data at $B = 8$ T to extract the asymmetric crossing points for the LLs. Figure 2(a) left panel shows this color plot, in which the crossing points are readily visible, such as that marked by the white arrow. From line traces along fixed n at particular filling factors (for example, $\nu = \pm 3$ shown in the right panel), we find and plot the D values at the crossings in Figure 2(b). For most filling factors, the crossing points have the same D magnitude but with their sign depending on the sign of ν . The exception is $\nu = \pm 2$, in which the $\nu = 2$ state crossing occurs at a smaller D value than $\nu = -2$.

To take initial steps towards understanding this behavior, following ref. 20, we assume a phenomenological single-particle model of SOC incorporating both an Ising term, $H_I = \frac{1}{2}\eta\lambda\sigma_z$ and a Rashba term, $H_R = \frac{1}{2}\lambda_R(\eta\sigma_xs_y - \sigma_ys_x)$, where λ is an energy scale describing the out-of-plane spin splitting caused by SOC, λ_R is an energy scale describing the in-plane Rashba SOC, the $\sigma_{x,y,z}$ are Pauli matrices for spin, $s_{x,y,z}$ are Pauli matrices for the A and B sublattices, and $\eta = +1$ for

states near the K point and -1 for the states near the K' point. All bilayer single particle parameters such as nearest neighbor and interlayer hopping are taken from ref. 20. We also add a Zeeman term $H_Z = -\frac{1}{2}E_Z\sigma_z$,²⁰ where $E_Z = g\mu_B B$ is the Zeeman energy with $g \approx 2$ the electron g -factor and μ_B the Bohr magneton, and we account for the interlayer potential u caused by D (LL energies vs. u for $B = 8$ T are plotted in Figure S4). When $D = 0$, all the degeneracies are lifted as a result of SOC coupling in both the model and in the data as shown in the Figure 1(c) upper panel. In contrast, in non-SOC BLG, K-K' degeneracy yields two doubly degenerate LLs in each quartet so that the gaps vanish for $\nu = \pm 5$ and ± 7 . Moreover, under inversion symmetry the crossing points are symmetric in D , which is not the case in the SOC device. Thus, the asymmetry in D and fully broken degeneracies are clear evidence of the inversion symmetry breaking caused by the presence of the WSe₂.

We now turn to quantitatively estimating λ and λ_R from the data. The crossing points for $\nu = \pm 3$ are expected to be unaffected by Coulomb interactions,²⁹ and are insensitive to the Rashba coupling.²⁰ The crossing points of $\nu = \pm 3$ are relatively insensitive to B [Figure 2(b)]. By comparison to the results of the single particle model, we infer that the K point spin splitting has spin down at higher energy than spin up, and vice versa at the K' point. This implies that $\lambda < 0$, which is predicted to occur for certain ranges of graphene-WSe₂ twist angles.³⁰ Such a negative λ is also indicated by the crossings for $\nu = 3$ and 5 having the same sign of D (see SI Figure S4). From these crossing points, we find $\lambda = -2.2$ meV.

For the Rashba coupling, expected to be positive regardless of twist angle,³⁰ we measure the crossing points' D -values for $\nu = \pm 5, \pm 6$, and ± 7 . Figure 2(c) plots this data for $B = 6$ T and Figure 2(d) plots the corresponding data for $B = 10$ T. Using $\lambda = -2.2$ meV as obtained above, and using λ_R as the only free parameter, we minimize the sum of all the squared deviations

between the predicted single particle values and the measured data, obtaining $\lambda_R \sim 20$ meV.

Figures 2(c) and 2(d) show the resulting model values using the best fit λ_R plotted as open triangles. The single particle model with this value of λ_R yields a reasonable agreement to the measured values. However, the crossing points are in principle still potentially affected by Coulomb interactions.

To elucidate the role of Coulomb interactions in the behavior of the system, we determine the transport gaps by measuring the temperature dependence of R_{xx} in a number of valleys vs. D . An example of this behavior is shown in Figure 3(a) which shows Arrhenius plots for $\nu = 6$ at $D = 0$ vs. B . We then fit the R_{xx} minima against $1/T$ with the equation $R = R_0 \exp\left[-\frac{\Delta - \Gamma}{2k_B T}\right]$ to extract the quantity $\Delta - \Gamma$, where Δ is the gap and Γ (full width at half maximum) is the Landau level width. Figure 3(b) shows the extracted $\Delta - \Gamma$ vs. B for $\nu = 5, 6$, and 7 .

To make a comparison to the single particle model above, we consider the rate of change of $\Delta - \Gamma$ with D [i.e. $d(\Delta - \Gamma)/dD = d\Delta/dD$ assuming constant Γ] near a gap closing. This is insensitive to Γ , as well as Coulomb interactions within a Hartree-Fock picture. Table 1 shows the measured values for a number of crossings. Values on both sides of the crossings are averaged if both are obtained. We then compute the expected $d\Delta/dD$ at each crossing, and using only λ_R as a free parameter minimize the sum of the squared differences between all the expected and measured crossing rates with respect to λ_R . We find a best fit value of $\lambda_R \approx 15$ meV for the data shown. The computed values using this λ_R value are tabulated in Table 1 column 4 which show reasonable agreement to the measured values. However, deviations exist which may, for example, stem from measurement uncertainty in the gap closing rates. This indicates that the λ_R

obtained from this method should be considered only an estimate characteristically ~ 15 meV, consistent with the range of previously found values, e.g. refs. 9 and 15.

Using this extracted value of λ_R , we compute the expected behavior of the $\nu = 5$ gap and plot it as the dashed line in Figure 3(b) without free parameters. Fitting a straight line to the $\nu = 5$ gap data in Figure 3(b) yields a slope of 0.11 ± 0.02 meV/T, very close to the theoretical slope of $\approx g\mu_B = 0.115$ meV/T, indicating that Coulomb interactions have only a small effect on the gap. The $\nu = 7$ gap is slightly larger, but similar in magnitude. On the other hand, the fitted slope of 0.245 meV/T of the $\nu = 6$ gap is significantly larger than $g\mu_B$, and also increases with B . In a single particle picture, the quartet of LLs associated with these gaps consists of states that can be labeled by a K or K' valley index and spin. The K and K' states are split by the SOC into nearly up and down spin states (with slight canting), which are oppositely directed in the two valleys, effectively. The single particle calculation shows that although the Rashba SOC reduces the total splitting, the $\nu = 5$ gap varies linearly with B with a slope $\approx g\mu_B$, as observed. The measured energy is lower than the predicted single particle splitting, which we attribute a LL width ~ 0.4 meV. The results of the single particle model for all three gaps $\nu = 5, 6$ and 7 are plotted over a wider range of B in the Figure 3(b) inset. While this picture produces reasonable results over the measured B range for Δ_5 and Δ_7 , it predicts that Δ_6 starts at a splitting set by the SOC, and decreases with B , contrary to what is observed.

We therefore consider a model that includes Coulomb interactions. SOC breaks the K-K' symmetry, leading to potentially different exchange energies in the two valleys. Additionally, there could be an exchange coupling between the K and K' states. However, based on the close agreement in the behavior of the Δ_5 and Δ_7 gaps to the single particle picture we assume this is negligible. Thus, we model the Coulomb interaction with two parameters, which are J_K and $J_{K'}$,

corresponding to the exchange energy to flip a spin within a LL in the K or K' valleys, with an effective single particle picture shown schematically in Figure 4(a). The similar energy scales measured for Δ_5 and Δ_7 indicate that $J_K \approx J_{K'}$. We obtain $J_{K'}$ by taking the total gap Δ_6 to be $\Delta_{6\text{-sp}} + J_{K'}$, where $\Delta_{6\text{-sp}}$ is the expected single particle gap at $D = 0$, plotted in the inset to Figure 4(b), and rearranging to find $J_{K'} = \Delta_6 - \Delta_{6\text{-sp}}$. Because of the unknown Coulomb interactions outside of the measured range and the uncertainty in the LL width, this quantity is plotted in Figure 4(b) as a differential $\Delta J_{K'}$ relative to its value at $B = 6$ T. The behavior is approximately linear in B . While it may be initially expected that $J_{K'}$ is proportional to the Coulomb energy scale $e^2/\epsilon l_B$, where l_B is the magnetic length and ϵ the dielectric constant, this result is in agreement with previous experiments that also find an approximately linear in B Coulomb interaction.^{31, 32} This may arise from changes to the dielectric constant with B .⁴² However, more work will be required to understand the origin of this behavior.

In sum, we have measured high mobility bilayer graphene samples in which the spin-orbit interaction is induced by proximity coupling to WSe₂. The Ising parameter is measured to be $\lambda \approx -2.2$ meV, while the Rashba parameter is ~ 10 meV. The SOC breaks all degeneracies of the LLs at $D = 0$, and while the crossing points vs. D are qualitatively in agreement with a single particle model, both the gaps and the crossing points can be affected by Coulomb interactions. We measure the Coulomb energy corrections for $\nu = 6$ and find it is approximately linear in B over the measured range, in accordance with previous results on non-SOC bilayer graphene. The quantum Hall effect is a useful probe of SOC in bilayer graphene. In future work, this approach may be used to test theories in which both the Ising and Rashba SOC are tunable by the twist angle between the graphene and WSe₂,^{30, 43} potentially affording a unique approach to controlling SOC in materials.

AUTHOR INFORMATION

Corresponding Author

*Email: bockrath.31@osu.edu

Funding Sources

This research funded by DOE ER 46940-DE-SC0010597. Growth of hexagonal boron nitride crystals was supported by the Elemental Strategy Initiative conducted by the MEXT, Japan, A3 Foresight by JSPS and the CREST(JPMJCR15F3), JST.

REFERENCES

1. Hasan, M. Z.; Kane, C. L., Colloquium: topological insulators. *Rev. Mod. Phys.* **2010**, *82* (4), 3045.
2. Manchon, A.; Koo, H. C.; Nitta, J.; Frolov, S.; Duine, R., New perspectives for Rashba spin-orbit coupling. *Nat. Mater.* **2015**, *14* (9), 871.
3. Boettger, J. C.; Trickey, S. B., First-principles calculation of the spin-orbit splitting in graphene. *Phys. Rev. B* **2007**, *75* (12), 121402.
4. Konschuh, S.; Gmitra, M.; Kochan, D.; Fabian, J., Theory of spin-orbit coupling in bilayer graphene. *Phys. Rev. B* **2012**, *85* (11), 115423.
5. van Gelderen, R.; Smith, C. M., Rashba and intrinsic spin-orbit interactions in biased bilayer graphene. *Phys. Rev. B* **2010**, *81* (12), 125435.
6. Sichau, J.; Prada, M.; Anlauf, T.; Lyon, T. J.; Bosnjak, B.; Tiemann, L.; Blick, R. H., Resonance Microwave Measurements of an Intrinsic Spin-Orbit Coupling Gap in Graphene: A Possible Indication of a Topological State. *Phys. Rev. Lett.* **2019**, *122* (4), 046403.
7. Balakrishnan, J.; Kok Wai Koon, G.; Jaiswal, M.; Castro Neto, A. H.; Özyilmaz, B., Colossal enhancement of spin-orbit coupling in weakly hydrogenated graphene. *Nat. Phys.* **2013**, *9*, 284.
8. Marchenko, D.; Varykhalov, A.; Scholz, M. R.; Bihlmayer, G.; Rashba, E. I.; Rybkin, A.; Shikin, A. M.; Rader, O., Giant Rashba splitting in graphene due to hybridization with gold. *Nat. Commun.* **2012**, *3*, 1232.
9. Wang, Z.; Ki, D.-K.; Khoo, J. Y.; Mauro, D.; Berger, H.; Levitov, L. S.; Morpurgo, A. F., Origin and Magnitude of 'Designer' Spin-Orbit Interaction in Graphene on Semiconducting Transition Metal Dichalcogenides. *Phys. Rev. X* **2016**, *6* (4), 041020.
10. Wang, Z.; Ki, D. K.; Chen, H.; Berger, H.; MacDonald, A. H.; Morpurgo, A. F., Strong interface-induced spin-orbit interaction in graphene on WS₂. *Nat. Commun.* **2015**, *6*, 8339.
11. Benítez, L. A.; Sierra, J. F.; Saverio Torres, W.; Arrighi, A.; Bonell, F.; Costache, M. V.; Valenzuela, S. O., Strongly anisotropic spin relaxation in graphene-transition metal dichalcogenide heterostructures at room temperature. *Nat. Phys.* **2018**, *14* (3), 303-308.

12. Avsar, A.; Tan, J. Y.; Taychatanapat, T.; Balakrishnan, J.; Koon, G. K. W.; Yeo, Y.; Lahiri, J.; Carvalho, A.; Rodin, A. S.; O'Farrell, E. C. T.; Eda, G.; Castro Neto, A. H.; Özyilmaz, B., Spin-orbit proximity effect in graphene. *Nat. Commun.* **2014**, *5*, 4875.
13. Yang, B.; Tu, M.-F.; Kim, J.; Wu, Y.; Wang, H.; Alicea, J.; Wu, R.; Bockrath, M.; Shi, J., Tunable spin-orbit coupling and symmetry-protected edge states in graphene/WS₂. *2D Mater.* **2016**, *3* (3), 031012.
14. Yang, B.; Lohmann, M.; Barroso, D.; Liao, I.; Lin, Z.; Liu, Y.; Bartels, L.; Watanabe, K.; Taniguchi, T.; Shi, J., Strong electron-hole symmetric Rashba spin-orbit coupling in graphene/monolayer transition metal dichalcogenide heterostructures. *Phys. Rev. B* **2017**, *96* (4), 041409.
15. Wakamura, T.; Reale, F.; Palczynski, P.; Guéron, S.; Mattevi, C.; Bouchiat, H., Strong Anisotropic Spin-Orbit Interaction Induced in Graphene by Monolayer WS₂. *Phys. Rev. Lett.* **2018**, *120* (10), 106802.
16. Zihlmann, S.; Cummings, A. W.; Garcia, J. H.; Kedves, M.; Watanabe, K.; Taniguchi, T.; Schönenberger, C.; Makk, P., Large spin relaxation anisotropy and valley-Zeeman spin-orbit coupling in WSe₂/graphene/h-BN heterostructures. *Phys. Rev. B* **2018**, *97* (7), 075434.
17. Asmar, M. M.; Ulloa, S. E., Symmetry-breaking effects on spin and electronic transport in graphene. *Phys. Rev. B* **2015**, *91* (16), 165407.
18. Gmitra, M.; Fabian, J., Graphene on transition-metal dichalcogenides: A platform for proximity spin-orbit physics and optospintronics. *Phys. Rev. B* **2015**, *92* (15), 155403.
19. Gmitra, M.; Fabian, J., Proximity Effects in Bilayer Graphene on Monolayer WSe₂: Field-Effect Spin Valley Locking, Spin-Orbit Valve, and Spin Transistor. *Phys. Rev. Lett.* **2017**, *119* (14), 146401.
20. Khoo, J. Y.; Levitov, L., Tunable quantum Hall edge conduction in bilayer graphene through spin-orbit interaction. *Phys. Rev. B* **2018**, *98* (11), 115307.
21. Khoo, J. Y.; Morpurgo, A. F.; Levitov, L., On-Demand Spin-Orbit Interaction from Which-Layer Tunability in Bilayer Graphene. *Nano Lett.* **2017**, *17* (11), 7003-7008.
22. Island, J.; Cui, X.; Lewandowski, C.; Khoo, J.; Spanton, E.; Zhou, H.; Rhodes, D.; Hone, J.; Taniguchi, T.; Watanabe, K., Spin-orbit driven band inversion in bilayer graphene by van der Waals proximity effect. *arXiv preprint arXiv:1901.01332* **2019**.
23. Rosenberger, M. R.; Chuang, H.-J.; McCreary, K. M.; Hanbicki, A. T.; Sivaram, S. V.; Jonker, B. T., Nano-“Squeegee” for the Creation of Clean 2D Material Interfaces. *ACS Applied Materials & Interfaces* **2018**, *10* (12), 10379-10387.
24. Weitz, R. T.; Allen, M. T.; Feldman, B. E.; Martin, J.; Yacoby, A., Broken-Symmetry States in Doubly Gated Suspended Bilayer Graphene. *Science* **2010**, *330* (6005), 812.
25. Velasco Jr, J.; Jing, L.; Bao, W.; Lee, Y.; Kratz, P.; Aji, V.; Bockrath, M.; Lau, C. N.; Varma, C.; Stillwell, R.; Smirnov, D.; Zhang, F.; Jung, J.; MacDonald, A. H., Transport spectroscopy of symmetry-broken insulating states in bilayer graphene. *Nat. Nanotech.* **2012**, *7*, 156.
26. Maher, P.; Wang, L.; Gao, Y.; Forsythe, C.; Taniguchi, T.; Watanabe, K.; Abanin, D.; Papić, Z.; Cadden-Zimansky, P.; Hone, J.; Kim, P.; Dean, C. R., Tunable fractional quantum Hall phases in bilayer graphene. *Science* **2014**, *345* (6192), 61.
27. Lee, K.; Fallahazad, B.; Xue, J.; Dillen, D. C.; Kim, K.; Taniguchi, T.; Watanabe, K.; Tutuc, E., Chemical potential and quantum Hall ferromagnetism in bilayer graphene. *Science* **2014**, *345* (6192), 58.

28. Pan, C.; Wu, Y.; Cheng, B.; Che, S.; Taniguchi, T.; Watanabe, K.; Lau, C. N.; Bockrath, M., Layer Polarizability and Easy-Axis Quantum Hall Ferromagnetism in Bilayer Graphene. *Nano Lett.* **2017**, *17* (6), 3416-3420.
29. Hunt, B. M.; Li, J. I. A.; Zibrov, A. A.; Wang, L.; Taniguchi, T.; Watanabe, K.; Hone, J.; Dean, C. R.; Zaletel, M.; Ashoori, R. C.; Young, A. F., Direct measurement of discrete valley and orbital quantum numbers in bilayer graphene. *Nat. Commun.* **2017**, *8* (1), 948.
30. David, A.; Rakyta, P.; Kormányos, A.; Burkard, G., Induced spin-orbit coupling in twisted graphene-TMDC heterobilayers: twistrionics meets spintronics. *arXiv preprint arXiv:1905.08688* **2019**.
31. Martin, J.; Akerman, N.; Ulbricht, G.; Lohmann, T.; Smet, J. H.; von Klitzing, K.; Yacoby, A., Observation of electron-hole puddles in graphene using a scanning single-electron transistor. *Nat. Phys.* **2007**, *4*, 144.
32. Shi, Y.; Lee, Y.; Che, S.; Pi, Z.; Espiritu, T.; Stepanov, P.; Smirnov, D.; Lau, C. N.; Zhang, F., Energy Gaps and Layer Polarization of Integer and Fractional Quantum Hall States in Bilayer Graphene. *Phys. Rev. Lett.* **2016**, *116* (5), 056601.
33. Wang, L.; Meric, I.; Huang, P. Y.; Gao, Q.; Gao, Y.; Tran, H.; Taniguchi, T.; Watanabe, K.; Campos, L. M.; Muller, D. A.; Guo, J.; Kim, P.; Hone, J.; Shepard, K. L.; Dean, C. R., One-Dimensional Electrical Contact to a Two-Dimensional Material. *Science* **2013**, *342* (6158), 614.
34. McCann, E.; Fal'ko, V. I., Landau-Level Degeneracy and Quantum Hall Effect in a Graphite Bilayer. *Phys. Rev. Lett.* **2006**, *96* (8), 086805.
35. Novoselov, K. S.; McCann, E.; Morozov, S. V.; Fal'ko, V. I.; Katsnelson, M. I.; Zeitler, U.; Jiang, D.; Schedin, F.; Geim, A. K., Unconventional quantum Hall effect and Berry's phase of 2π in bilayer graphene. *Nat. Phys.* **2006**, *2*, 177.
36. Zhao, Y.; Cadden-Zimansky, P.; Jiang, Z.; Kim, P., Symmetry Breaking in the Zero-Energy Landau Level in Bilayer Graphene. *Phys. Rev. Lett.* **2010**, *104* (6), 066801.
37. Dean, C. R.; Young, A. F.; Meric, I.; Lee, C.; Wang, L.; Sorgenfrei, S.; Watanabe, K.; Taniguchi, T.; Kim, P.; Shepard, K. L.; Hone, J., Boron nitride substrates for high-quality graphene electronics. *Nat. Nanotech.* **2010**, *5*, 722.
38. Young, A. F.; Dean, C. R.; Wang, L.; Ren, H.; Cadden-Zimansky, P.; Watanabe, K.; Taniguchi, T.; Hone, J.; Shepard, K. L.; Kim, P., Spin and valley quantum Hall ferromagnetism in graphene. *Nat. Phys.* **2012**, *8*, 550.
39. Alicea, J.; Fisher, M. P. A., Graphene integer quantum Hall effect in the ferromagnetic and paramagnetic regimes. *Phys. Rev. B* **2006**, *74* (7), 075422.
40. Lambert, J.; Côté, R., Quantum Hall ferromagnetic phases in the Landau level $N=0$ of a graphene bilayer. *Phys. Rev. B* **2013**, *87* (11), 115415.
41. Li, J.; Tupikov, Y.; Watanabe, K.; Taniguchi, T.; Zhu, J., Effective Landau Level Diagram of Bilayer Graphene. *Phys. Rev. Lett.* **2018**, *120* (4), 047701.
42. Shizuya, K., Structure and the Lamb-shift-like quantum splitting of the pseudo-zero-mode Landau levels in bilayer graphene. *Phys. Rev. B* **2012**, *86* (4), 045431.
43. Li, Y.; Koshino, M., Twist-angle dependence of the proximity spin-orbit coupling in graphene on transition-metal dichalcogenides. *Phys. Rev. B* **2019**, *99* (7), 075438.

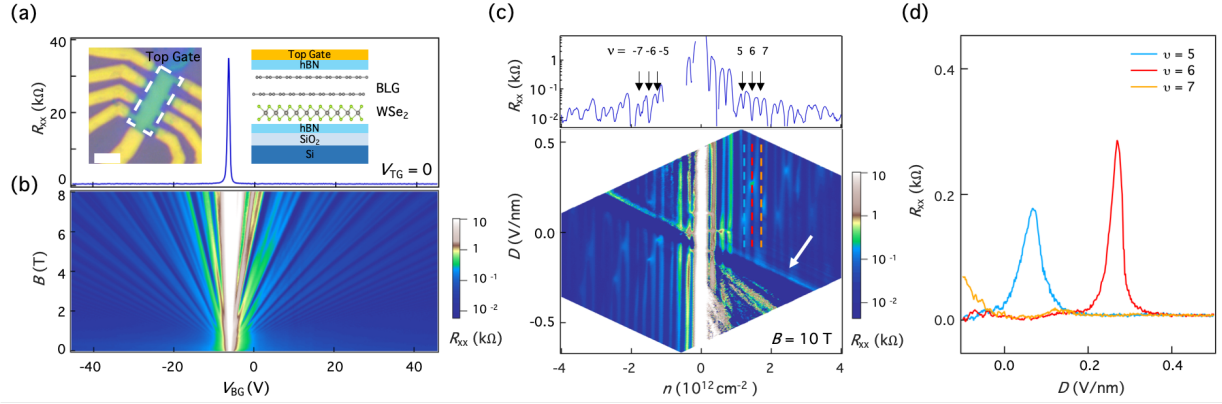


Figure 1. Device structure and SOC modified LL properties. (a) Main panel: R_{xx} vs. bottom gate voltage V_{BG} at $T = 1.5$ K with top gate voltage $V_{TG} = 0$. Left inset: Optical image of a BLG/WSe₂ device. The dashed outline indicates the top gated region before metalization. Scale bar is $2 \mu\text{m}$. Right inset: Schematic diagram of the layer stack. (b) R_{xx} vs. V_{BG} and magnetic field B showing a Landau Fan pattern. Quantum Hall states at all integer filling factors of the Landau levels are clearly visible due to the full degeneracy lifting. (c) Top panel: R_{xx} vs. n at $D = 0$. Bottom panel: Color plot of R_{xx} vs. n and D at $B = 10$ T. (d) Vertical line cuts passing Landau Level crossing points along the dashed lines in panel c. Each curve represents a fixed filling factor for $\nu = 5, 6,$ and 7 .

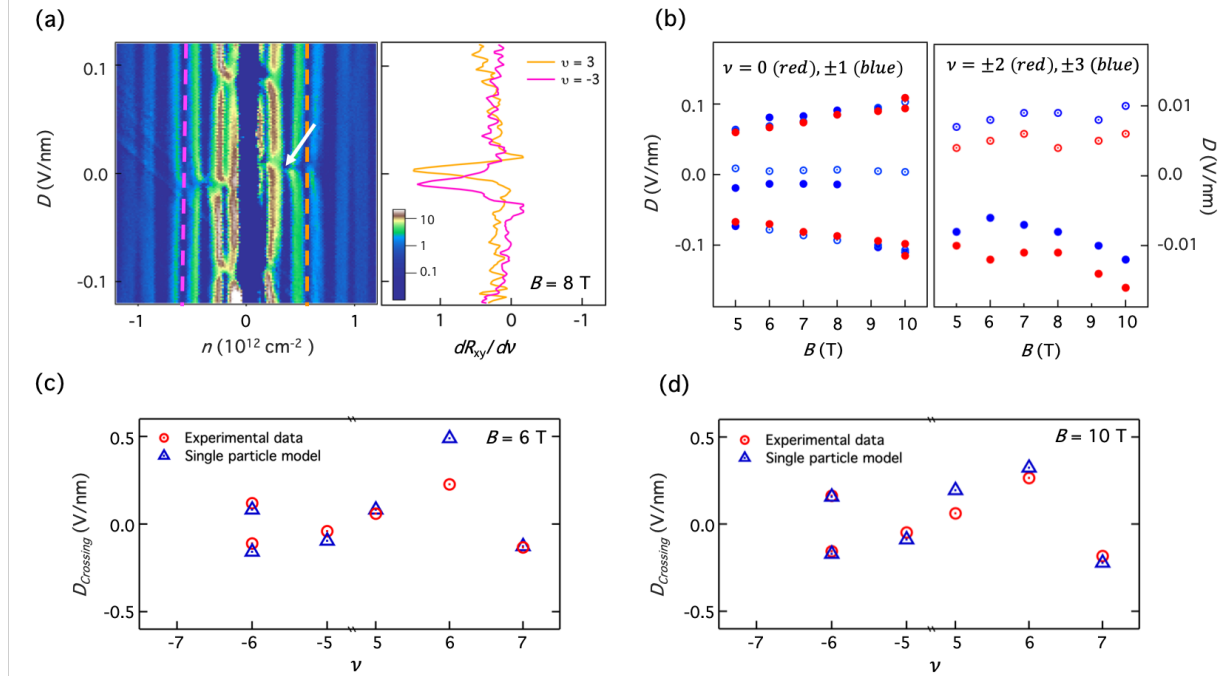


Figure 2. Transitions at zeroth Landau level. (a) Left panel: dR_{xy}/dv vs. n and D at $B = 8 \text{ T}$. Right panel: Vertical line cuts passing LL crossing points along the dashed lines in the left panel at $\nu = \pm 3$. Maxima indicate the crossing points. (b) Measured D values of LL crossing points vs. B for $N = 0$ and 1. Open/filled circles stand for positive/negative filling factors. (c) and (d) show a comparison between measured LL crossing points and our simulated values from the single particle model at $B = 6 \text{ T}$ and 10 T , respectively. [Crossing points at $B = 6 \text{ T}$ are extracted from SI Figure S2(a).]

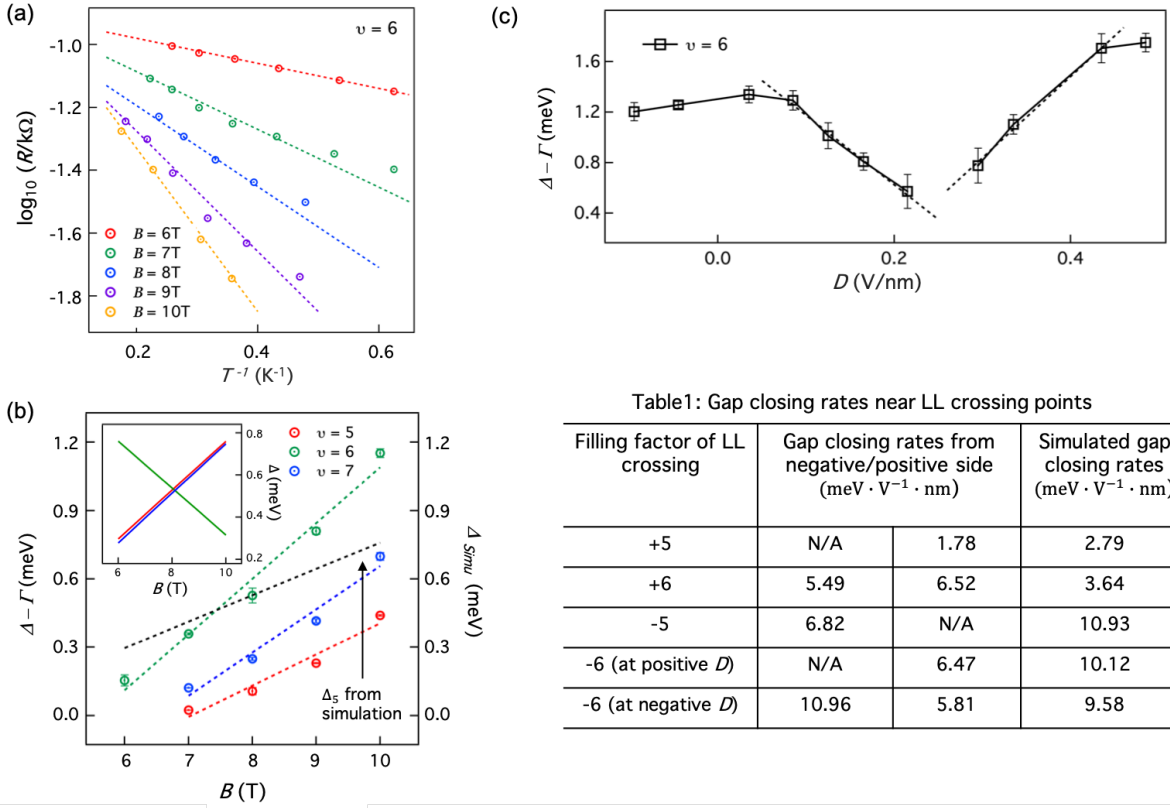


Figure 3. LL energies and broken symmetry gaps in a BLG/WSe₂ system. (a) Thermal activation plots at various B values for $\nu=6$ states at $D=0$. (b) Measured thermal activation gaps $\Delta - \Gamma$ vs. B at $D=0$ for $\nu=5, 6$, and 7 , where Γ is the LL width (left axis). Dotted lines are linear fits of gap sizes vs. B . The black dotted line stands for simulated gap size for $\nu=5$ without broadening (right axis). Inset: single particle model for all three gaps $\nu=5, 6$ and 7 . Measured gaps $\Delta - \Gamma$ vs. D at $B=10$ T for $\nu=6$. The missing data points are at the LL crossing point. By fitting the slopes of the gap changes with D (dashed lines), we extract gap closing rates near LL crossing points and compare them with simulated values, as shown in Table 1. (Gap closing rates for other filling factors in addition to $\nu=6$ are extracted from data shown in SI Figure S5.)

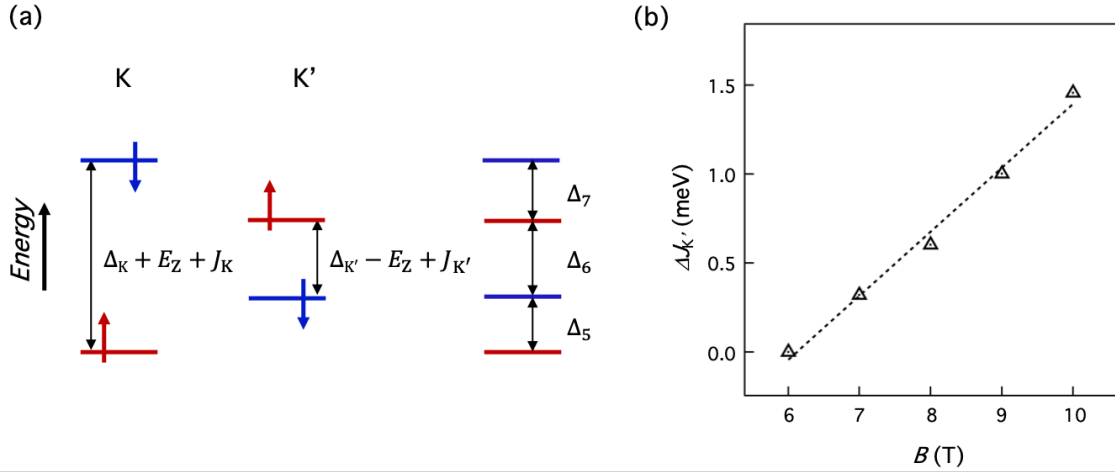


Figure 4. Corrections to the single particle model due to Coulomb interactions. (a) Schematic representation of the broken symmetry gaps for $N=2$ at $D=0$. Δ_K and $\Delta_{K'}$ stands for the proximity induced Ising and Rashba SOC, causing different splitting in K and K' valleys. J_K and $J_{K'}$ are the Coulomb interactions for the electrons with opposite spins in the same valley. (b) Extracted differential $\Delta J_{K'}$ relative to its value at $B=6$ T, at $D=0$.

Supporting Information

Quantum Hall Effect Measurement of Spin-Orbit Coupling Strengths in Ultraclean Bilayer Graphene/WSe₂ Heterostructures

*Dongying Wang¹, Shi Che¹, Guixin Cao¹, Rui Lyu², Kenji Watanabe³, Takashi Taniguchi³, Chun
Ning Lau¹, Marc Bockrath^{1*}*

¹Department of Physics, The Ohio State University, Columbus, OH 43210, USA

²Department of Physics and Astronomy, University of California, Riverside, CA 92521, USA

³ National Institute for Materials Science, Namiki Tsukuba Ibaraki 305-0044 Japan.

KEYWORDS: graphene, transition-metal dichalcogenide, spin-orbit coupling, quantum transport

*Email: bockrath.31@osu.edu

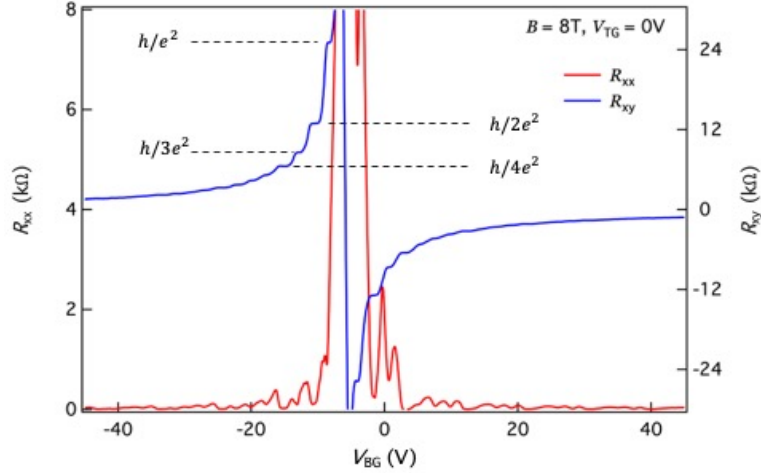


Figure S1. Integer quantum Hall effect at $B = 8$ T. Line cuts from the Landau fan color plot. Integer filling factor features with unit increment, minima in R_{xx} (red) and plateaus in R_{xy} (blue), are visible.

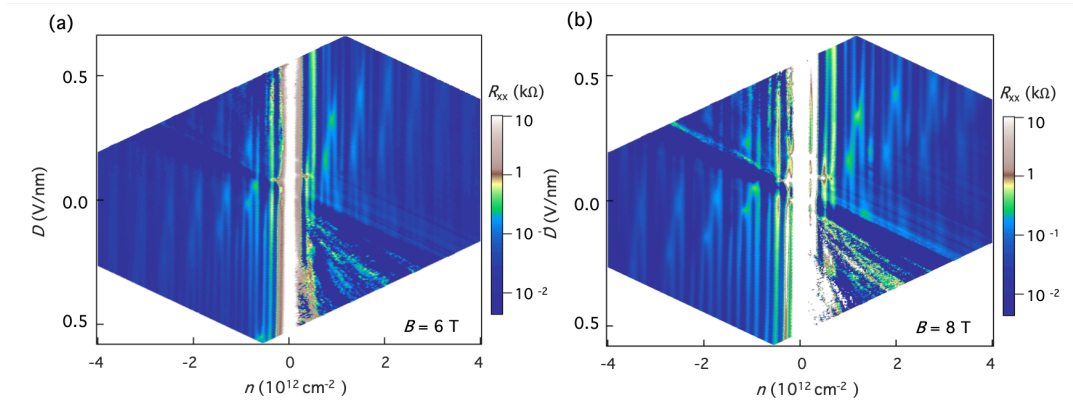


Figure S2. Color plot of R_{xx} vs. n and D at different magnetic fields. R_{xx} measurements at additional values of B , such as (a) 6T and (b) 8T, in addition to the 10T data we displayed in the main text.

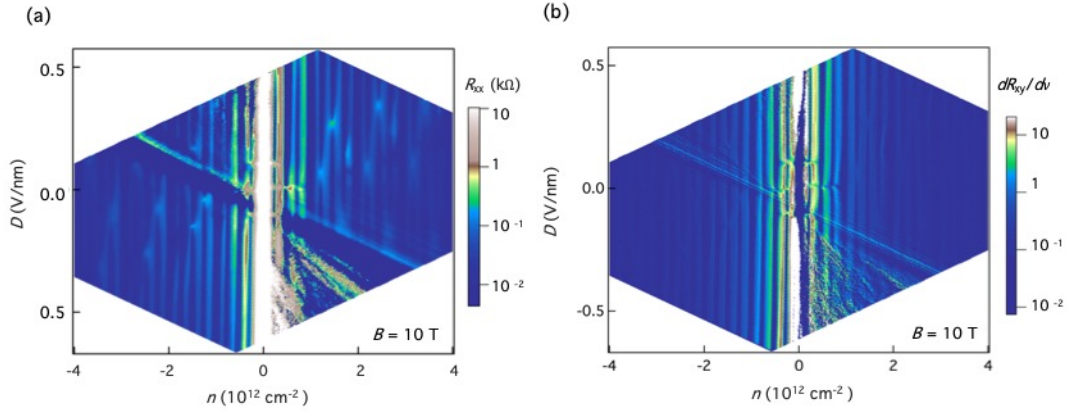


Figure S3. LL crossing features in color maps of R_{xx} and dR_{xy}/dv . (a) Color plot of R_{xx} vs. n and D at $B = 10 \text{ T}$. (b) Color plot of dR_{xy}/dv vs. n and D at $B = 10 \text{ T}$. From two separate plots, we are able to extract the same information for LL crossings. However, the latter shows the quantum Hall features more clearly, which enable us to extract data more accurately.

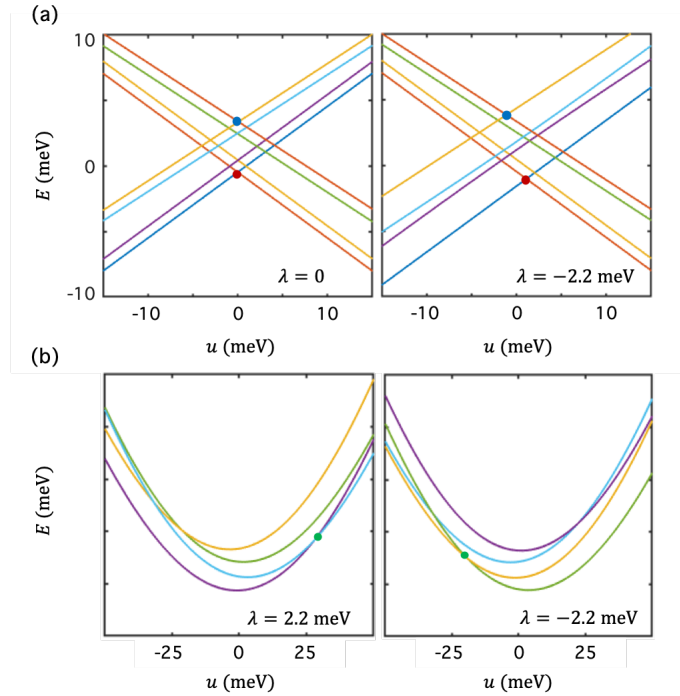


Figure S4. Energy level diagram in single particle simulations of (a) Nearly degenerate zero-energy LLs in absence (left) and with (right) Ising type SOC at $B = 8 \text{ T}$. The blue and red dots indicate the crossings for $\nu = +3$ and -3 , respectively. By comparing the positions of crossing we extract from experimental data [see Figure 3(a)] with simulated results, we find the best fit for value of Ising type SOC is $\lambda = -2.2 \text{ meV}$. (b) $N = 2$ LLs with positive (left) and negative (right)

Ising type SOC at $B = 10\text{T}$. The green dots indicate the crossings for $\nu = 5$. By comparing the signs of crossing of $\nu = 3$ and 5, we can further confirm that the Ising type SOC is $\lambda = -2.2\text{ meV}$.

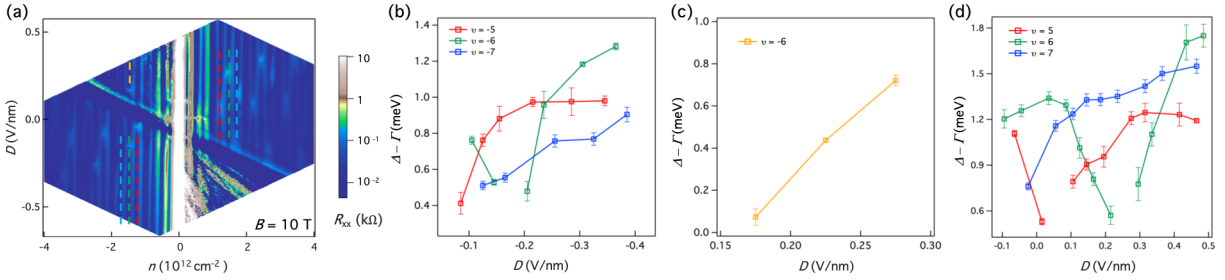


Figure S5. Displacement field dependence of $N = 2$ QHs. (a) Color plot of R_{xx} vs. n and D at $B = 10\text{ T}$. (b) and (c) Measured gaps $\Delta - \Gamma$ vs. D at $B = 10\text{ T}$ for $\nu = -5, -6, -7$ at negative and positive displacement fields. (d) Measured gaps $\Delta - \Gamma$ vs. D at $B = 10\text{ T}$ for $\nu = 5, 6, 7$ at negative and positive displacement fields. The missing data points are located at LL crossing points. As discussed in the main text, by fitting the slopes of the gap changes with D , we extract gap closing rates near LL crossing points and compare them with simulated values.